Article:
Smith, J.A. orcid.org/0000-0001-6889-4408, Game, O.S. orcid.org/0000-0002-5573-3602, Bishop, J.E. et al. (13 more authors) (2020) Rapid scalable processing of tin oxide transport layers for perovskite solar cells. ACS Applied Energy Materials, 3 (6). pp. 5552-5562. ISSN 2574-0962

https://doi.org/10.1021/acsaem.0c00525

ACS APPLIED ENERGY MATERIALS

www.acsaem.org Article

Rapid Scalable Processing of Tin Oxide Transport Layers for Perovskite Solar Cells

Joel A. Smith, Onkar S. Game, James E. Bishop, Emma L. K. Spooner, Rachel C. Kilbride, Claire Greenland, Rahul Jayaprakash, Tarek I. Alanazi, Elena J. Cassella, Alvaro Tejada, Ganna Chistiakova, Michael Wong-Stringer, Thomas J. Routledge, Andrew J. Parnell, Deborah B. Hammond, and David G. Lidzey*

Cite This: https://dx.doi.org/10.1021/acsaem.0c00525 Read Online

ACCESS | Metrics & More | Article Recommendations | Supporting Information

ABSTRACT: The development of scalable deposition methods for perovskite solar cell materials is critical to enable the commercialization of this nascent technology. Herein, we investigate the use and processing of nanoparticle SnO_2 films as electron transport layers in perovskite solar cells and develop deposition methods for ultrasonic spray coating and slot-die coating, leading to photovoltaic device efficiencies over 19%. The effects of postprocessing treatments (thermal annealing, UV ozone, and O_2 plasma) are then probed using structural and spectroscopic techniques to characterize the nature of the np-SnO_2/perovskite interface. We show that a brief "hot air flow" method can be used to replace extended thermal annealing, confirming that this approach is compatible with high-throughput processing. Our results highlight the importance of interface management to minimize nonradiative losses and provide a deeper understanding of the processing requirements for large-area deposition of nanoparticle metal oxides.

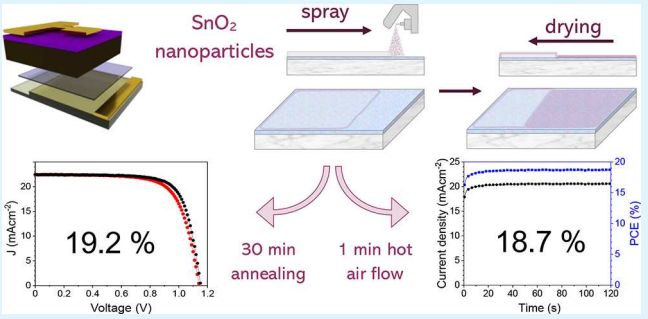

KEYWORDS: *tin oxide, perovskite solar cells, scalable processing, spray-coating, SnO_2, interfaces*

INTRODUCTION

Organic−inorganic hybrid perovskite materials have generated excitement and extensive research interest in the photovoltaic community since their demonstration in 2009, with the record single-junction power conversion efficiency (PCE) now reaching above 25%.[1,2] This has been made possible by a distinctive set of characteristics in this family of materials, including high optical absorption, long charge-carrier lifetimes enabled by low nonradiative recombination rates, and extensive possibilities for compositional tuning.[3,4] Typically, high efficiency n−i−p cell architectures have relied on a compact and mesoporous TiO_2 electron transport layer (ETL) architecture.[5] However, a primary concern with TiO_2 is the inherent instability caused by UV light interacting with molecular O_2 adsorbed at surface defect sites. This process may then lead to decomposition of the organic component of the active layer, with many stability studies on devices utilizing TiO_2 typically making use of UV filters to negate such effects.[6,7] TiO_2-based systems also commonly require processing steps at temperatures above 450 °C.[5] This temperature is, however, incompatible with many roll-to-roll (R2R) or sheet-to-sheet substrates such as polyethylene terephthalate (PET) and will also limit their use in tandem devices that may have other temperature-sensitive layers.

One approach to mitigate ETL UV instability and reduce the processing temperature is to replace TiO_2 (band gap ∼3.3 eV) with a wider band gap metal oxide such as SnO_2 (3.6−4.2 eV), with the wider band gap also reducing parasitic absorption.[8,9] Compared to TiO_2, crystalline SnO_2 exhibits nearly 2 orders of magnitude higher electron mobility;[10] a property that suggests it should act as a highly effective ETL. Atomic layer deposition (ALD) has been used to deposit amorphous SnO_2, and it is thought that its conduction band is well aligned for barrier-free electron transfer from various perovskites.[11] Various routes have been used to deposit planar SnO_2 including chemical bath deposition (CBD), sol−gel conversion,[12] chemical vapor deposition (CVD),[13] plasma-enhanced ALD,[14] electron-beam evaporation,[15] thermal evaporation,[16] sputtering,[17] spin-coated

Received: March 12, 2020
Accepted: May 7, 2020
Published: May 8, 2020

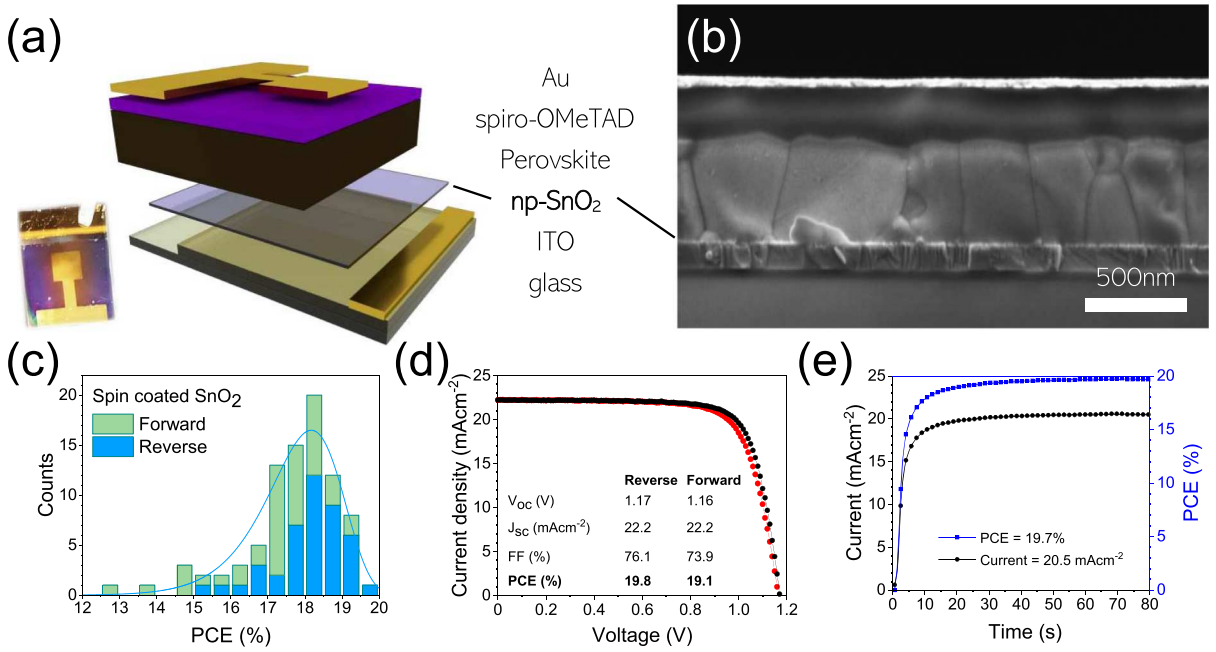

Figure 1. np-SnO_2 device structure and performance. (a) Illustration of the n−i−p layer architecture with a photograph of a completed device inset. (b) Cross-sectional SEM image of a completed device showing densely packed perovskite grains and ultrathin np-SnO_2 layer. (c) Histogram of all spin-coated device efficiencies (forward and reverse sweep), showing excellent reproducibility. Champion cell performance is illustrated by (d) a current−voltage sweep and (e) stabilized device performance at the J−V determined MPP.

sol−gel precursor in combination with CBD,[18] nanoparticle routes,[19,20] and mesoporous SnO_2.[21,22] Importantly, mesoporous SnO_2 has also been demonstrated to have improved UV stability relative to mesoporous TiO_2, although it has so far been processed at high temperature, preventing the use of fluorine−SnO_2 (FTO) layers because of fluorine migration.[21,22] Two key papers on planar SnO_2-only ETL deposition routes have reported efficiencies of over 20%,[18,19] with the work by Jiang *et al.* using an off-the-shelf nanoparticle SnO_2 (np-SnO_2) product subsequently leading to a record-breaking planar n−i−p device PCE of 23.3%.[23] This np-SnO_2 system has the advantage of not undergoing temperature-sensitive phase formation during annealing, which can impact the reproducibility of other SnO_2 ETL deposition processes.

In this paper, we utilize an np-SnO_2 system with a triple cation, mixed-halide perovskite[5] with solution composition $Cs_{0.05}FA_{0.79}MA_{0.16}PbI_{2.45}Br_{0.55}$ and demonstrate highly reproducible stabilized power output (SPO) efficiencies of up to 19.7% and good batch-to-batch reproducibility. We explore two scalable np-SnO_2-coating methods (spray-coating and slot-die coating) and achieve peak PCEs of over 18% SPO. To demonstrate a rapid process compatible with R2R manufacture, we investigate both annealing-free and hot air flow (HAF) flash drying processes (120 °C for 1 min) combined with other low-temperature post-treatments (ultraviolet-ozone (UVO) and O_2 plasma) to replace or reduce the commonly used annealing step (10−30 min at 150 °C).[19,24] Using such techniques, we develop a rapid process that combines spray-coating, HAF at 120 °C, and UVO treatment to achieve 18.7% SPO using a fully scalable ETL deposition process. These results demonstrate the benefit of *ex situ*-crystallized nanoparticle metal oxides for achieving efficient, rapidly processed photovoltaic devices.

RESULTS AND DISCUSSION

Electron Transport Layer Deposition. To establish a stable baseline for experiments using more scalable techniques, we explored the fabrication of perovskite solar cell (PSC) devices in which the ETL was deposited by spin-coating np-SnO_2 from a diluted commercially available dispersion. Full details of the techniques used are given in Experimental Methods. Figure 1 shows the n−i−p configuration of the device, together with a scanning electron micrograph (SEM) cross-section of a completed device. Here, the full device structure is as follows: indium tin oxide (ITO), np-SnO_2 ETL, triple cation perovskite $Cs_{0.05}FA_{0.79}MA_{0.16}PbI_{2.45}Br_{0.55}$ absorbing layer, doped spiro-OMeTAD hole transport layer (HTL), and Au top contact.

We achieved a narrow distribution of device efficiencies on ITO for large 0.16 cm^2 cells (see Figure 1c), with a champion device PCE of 19.8% reverse sweep (V_{OC} to J_{SC}) efficiency (Figure 1d) with the stabilized power output (SPO) closely matching the reverse sweep PCE at 19.7% (see Figure 1e). The batch-to-batch reproducibility and device metrics are promising; multiple devices were realized with a V_{OC} of 1.17 V, corresponding to a voltage loss of 0.45 eV from the 1.62 eV band gap in the best cells (Figure S1). Comparable efficiencies of up to 18.8% were demonstrated for smaller devices fabricated on fluorine-doped tin oxide (FTO) substrates (see Figure S2). For comparison, we also show data in Figure S3 for small cells fabricated using the $SnCl_4{\cdot}5H_2O$ spin-coating method proposed by Ke *et al.* and developed by Anaraki *et al.*[8,18] Here, we found similar performance in some devices; however, we find the process to have low reproducibility (a broader distribution compared to np-SnO_2 devices in Figure S2), with full cell performance parameters given in Table S1. The process also requires a drying step at 100 °C followed by a longer annealing time at higher temperature (180 °C for 60 min).[18] Taken together, we believe that the low reproduci-

https://dx.doi.org/10.1021/acsaem.0c00525
ACS Appl. Energy Mater. XXXX, XXX, XXX−XXX

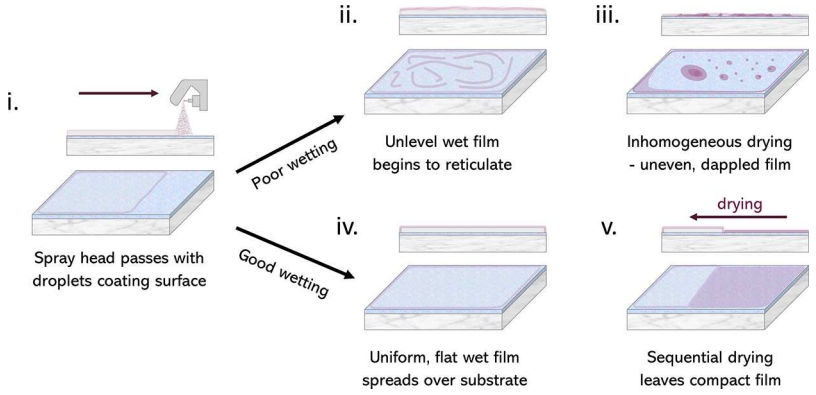

Figure 2. Scheme illustrating the optimized np-SnO_2 drying process across the UVO-treated ITO surface: (i) spray-coating, (ii) fast reticulation, (iii) dry film with poor uniformity, (iv) ideal wet film, and (v) drying proceeds across the substrate.

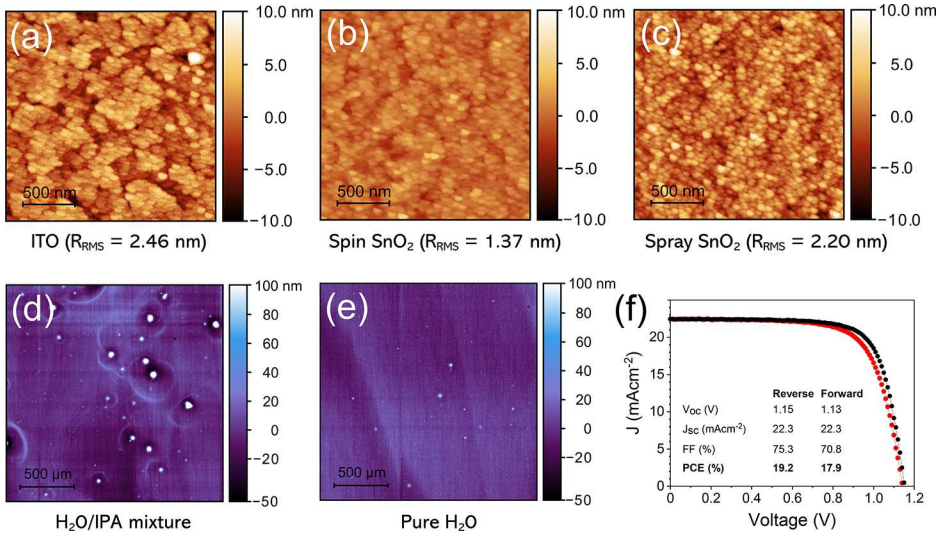

Figure 3. AFM height maps for uniformity and roughness of (a) ITO, (b) spin-coated and (c) spray-coated np-SnO_2 layers. Profilometric mapping of completed devices using spray-deposited np-SnO_2 with (d) IPA/H_2O mixed solvent and (e) H_2O-only solution; here, np-SnO_2 layer inhomogeneity in the IPA/H_2O cast film leads to pinholes in subsequent layers. (f) *J*−*V* curve for the best-performing spray np-SnO_2 device.

bility, and temperature requirements to convert to SnO_2, makes the $SnCl_4{\cdot}5H_2O$ conversion process unsuitable for use in scalable device architectures, with nanoparticle metal oxides being an attractive solution for rapid processing.

Slot-Die Coating. Two scalable deposition methods were investigated to deposit the ETL layer. Slot-die coating is widely used in industrial R2R processes and has the key benefit of minimal material wastage during coating.[25,26] To deposit a range of thicknesses, we used a set solution concentration and flow speed and then explored a range of head speeds. Surface wetting was enhanced by UVO treating the ITO prior to deposition, with a 3 wt % np-SnO_2 solution prepared by diluting with H_2O. Improved wetting for contact coating methods can also be promoted by mixing the primary solvent with ethanol by dropwise addition.[26] We note that when diluting using only H_2O (which has a high surface tension of >70 mN m^{-1} at RT), a meniscus forms around the slot die head and at the substrate edges. Here, we mitigated this effect by placing the target substrate between two other substrates to ensure a uniform flow across the intended device area (see Figure S4), with the meniscus defining the thickness of the deposited layer (found to be ∼38 nm see Figure S5). This is confirmed by process optimization results, showing device efficiencies that are comparable across a range of head speeds from 3 to 15 mm s^{-1} (see Figure S6a). Champion and average device performance metrics are shown in Table S1 for all devices in both sweep directions, with a maximum PCE of 18.5% and only mild hysteresis for the reverse sweep direction (Figure S6b).

Spray Coating. As a non-contact scalable deposition technique, spray-coating offers the benefit of higher throughput than is achievable using slot-die or other contact coating methods.[27] However, care must be taken to ensure good wetting of the substrate, the formation of a uniform, leveled wet film and homogenous drying. In the case of perovskite films, solvent optimization is particularly critical as it is also necessary to control nucleation and crystallization behavior. This can be achieved through careful post-deposition treatments such as vacuum exposure,[28] a technique that has also been used in inkjet printing.[29] For the methods outlined here, we are using an ultrasonic spray coater, which atomizes the coating solution using a piezoelectric transducer into droplets from a moving head, which are directed with gas flow onto a static coating surface.[27] Here, we have adopted a single-pass coating approach, operating in ambient conditions and using nontoxic solvents.

https://dx.doi.org/10.1021/acsaem.0c00525
ACS Appl. Energy Mater. XXXX, XXX, XXX−XXX

Table 1. Champion Device Performance Metrics for Spin- and Spray-Coated np-SnO_2 Devices, with Average and Standard Deviation in Parenthesis[a]

coating	treatment	sweep	PCE (%)	J_{SC} (mA cm^{-2})	V_{OC} (V)	FF (%)	no. of cells
spin	annealed +15 min UVO	forward	19.29 (17.21 ± 1.40)	22.93 (22.13 ± 0.43)	1.16 (1.12 ± 0.03)	75.30 (69.23 ± 4.80)	43
		reverse	19.82 (18.17 ± 0.97)	22.94 (22.15 ± 0.46)	1.17 (1.13 ± 0.03)	76.14 (72.58 ± 2.38)	
spray	annealed +15 min UVO	forward	17.86 (16.62 ± 1.75)	22.26 (22.13 ± 0.26)	1.13 (1.13 ± 0.01)	70.76 (66.24 ± 6.13)	13
		reverse	19.22 (18.45 ± 1.18)	22.29 (22.19 ± 0.20)	1.15 (1.14 ± 0.01)	75.27 (72.76 ± 3.75)	
spray	annealed + delayed 15 min UVO	forward	14.92 (11.32 ± 2.68)	22.21 (22.01 ± 0.20)	1.01 (0.94 ± 0.09)	66.28 (53.76 ± 8.73)	13
		reverse	17.01 (15.08 ± 3.18)	22.39 (22.11 ± 0.23)	1.06 (1.00 ± 0.11)	72.38 (67.09 ± 10.07)	

[a]All devices use np-SnO_2 layers which were thermally annealed (150 °C for 30 min) and post-treated with UVO. Performance for spray-coated cells with np-SnO_2 layers left in air for 2 days following annealing is also shown, highlighting the issue of loss of performance resulting from surface contamination.

Typically, low surface tension and low boiling point solvents are used for spray-coating. When using H_2O as a solvent to spray-coat SnO_2, its high surface tension can lead to the formation of thick wet films despite its good wetting properties (indeed 30 s of UVO exposure is sufficient to encourage complete wetting, see Figure S7). The thickness of the wet film is also dictated by the volume of solution that lands on the substrate, the surface energy of the substrate, and meniscus effects at the edge of the substrate. We have optimized the spray-deposition process to deposit SnO_2 films on ITO glass and find that the use of a low concentration solution (1:70 np-SnO_2/H_2O), together with a UVO treatment leads to the formation of a homogeneous wet film. From this wet film, drying proceeds over the substrate surface in around 60 s. We show this process schematically in Figure 2, with further images and uniform conformal coatings shown in Figure S8. We note that in an industrial process, drying could be further controlled by use of an air-blade[24] or HAF across the surface, a process that we describe later.

Topography and Device Performance. To investigate the uniformity and roughness of the deposited films, we performed atomic force microscopy (AFM) on spin- and spray-coated np-SnO_2 (see Figure 3a−c). We found that spin coating significantly reduced the film root mean square surface roughness (R_{RMS}) from 2.46 nm for the uncoated ITO to 1.37 nm, with the spray-coated film being slightly rougher (R_{RMS} = 2.20 nm). Examining the topography of the coated surfaces, we find that the np-SnO_2 film (prepared using both deposition techniques) significantly reduces the surface density of voids in the ITO. We have compared spin- and slot-die-coated surfaces and find that slot-die-coated np-SnO_2 films exhibit comparable roughness to spin-coated films (1.37 nm) with annealing having little effect on film morphology (see Figure S9). We find that the spray-coated films have a reduced layer thicknesses, which is ∼17 nm (measured by spectroscopic ellipsometry), with this thickness being apparently insensitive to spray-coater head speed (see Figure S5). We speculate that this thin-sprayed np-SnO_2 film dries conformally over the surface, with its greater roughness possibly reflecting the roughness of the underlying ITO (see Figure 2).

We have also performed surface profilometry mapping on completed devices (glass/ITO/np-SnO_2/perovskite/spiro-OMeTAD/Au) to explore film morphology over larger length scales (2.5 mm × 2.5 mm). A surface map is shown in Figure 3d that was recorded from the surface of a device incorporating a spray-coated np-SnO_2 layer deposited from an IPA/H_2O/np-SnO_2 solvent mixture, with similar mixtures having been used with slot-die coating to improve wetting.[26] However, we found that de-mixing of this two-solvent system occurs during the atomization process in the ultrasonic spray head, as illustrated in Figure S10. Consequently, this poor uniformity bottom layer leads to a significant number of pinholes, with ring-like morphological defects resulting from undulations in the np-SnO_2 layer apparently propagating through subsequent layers in the completed device. However, this behavior can be largely suppressed by judicious choice of the spray solvent. Here, Figure 3e shows a topographic image of a device surface in which the np-SnO_2 was spray-coated with only H_2O solvent, leading to a greatly reduced density of pinholes and no ring-like features evident. This result highlights the different challenges with solvent engineering for spray coating as compared to contact methods; further details on creating stable solvent mixtures for spray-coating are given in Supporting Information note 1.

Device performance metrics for all devices are shown in Table 1. For optimized spray-coated np-SnO_2 devices, we achieved a champion PCE of 19.2% with a SPO for the best-performing cell of 18.6% (see Figure S11). We find that devices fabricated using a spray-coated np-SnO_2 layer exhibit increased $J-V$ hysteresis, a result consistent with a reduced uniformity in layer thickness. Despite this, we find that other performance metrics for spray-coated and slot-die-fabricated devices closely match those of average spin-coated cells.

We note that it is imperative to use the np-SnO_2 films directly after the application of annealing and UV ozone treatments. We observed that leaving annealed np-SnO_2 films in ambient conditions, even if subject to a UVO treatment directly before coating with perovskite, leads to a substantial loss in V_{OC} (see Table 1). This effect most likely results from the adsorption of organic species at the surface that cannot be effectively removed through the UVO treatment alone.

Scalable Processing. The methods outlined so far have utilized an annealing step of 150 °C for 30 min to dry, crystallize, and remove the solvent from the np-SnO_2 layer. However, such an extended thermal treatment is incompatible with rapid R2R or continuous processing, where the duration of the longest process dictates the maximum web speed. Furthermore, our standard process also involves a UVO surface preparation treatment for 15 min to increase the surface energy for perovskite wetting and remove surface contaminants. In the following sections, we describe techniques that we have developed to reduce process time and temperature, while maintaining good device performance.

Effect of Thermal Annealing. To minimize the cost and duration of film processing, it is desirable to remove the transport layer thermal annealing step. Fortunately, as the

https://dx.doi.org/10.1021/acsaem.0c00525
ACS Appl. Energy Mater. XXXX, XXX, XXX−XXX

SnO_2 nanoparticle system is already composed of precrystallized nanoparticle domains, there is no phase change or oxidation process required to form the SnO_2 phase. However, it is necessary to understand the effects played by any thermal treatments and UVO exposure on the transport layer and the SnO_2/perovskite interface. Previous reports on the optical absorption of np-SnO_2 suggest a band gap of 3.79−3.94 eV for annealed np-SnO_2 films, but with only a limited wavelength range below the band gap, required for accurate fitting.[19,30] Tauc-like plots from our transmission measurements indicate optical band gap values of 4.43 eV for non-annealed films and 4.39 eV for 150 °C annealed np-SnO_2 films (Figure S12). These values are significantly higher than those typically expected for phase-pure SnO_2, so we applied a band-fluctuations fitting model to spectroscopic ellipsometry data.[31] This confirmed the apparent wide optical band gap of 4.48 and 4.45 eV for as-deposited and thermally annealed films, respectively (see Table S2); this model is discussed in Supporting Information note 2.

Grazing incidence small-angle X-ray scattering (GISAXS) techniques can provide a wealth of information about the thin-film material structure and has been used extensively for characterization of photovoltaic materials. Here, we collected 2D X-ray scattering patterns of np-SnO_2 films (see Figure S13) and fitted an empirical Guinier−Porod model[32] to in-plane cuts through this data (see Figure 4) to investigate changes

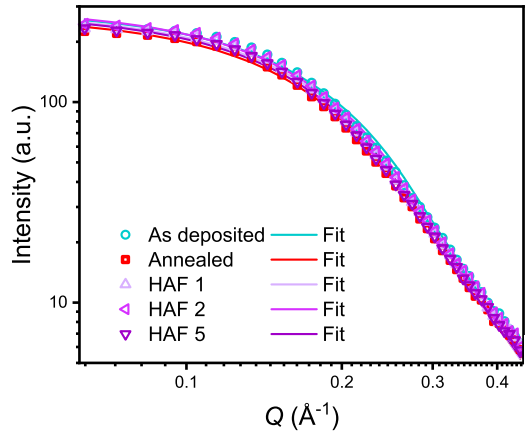

Figure 4. In-plane linecuts and Guinier−Porod fitting of GISAXS from np-SnO_2 layers with different annealing conditions; as-deposited, 30 min 150 °C annealed, and HAF for 1, 2, and 5 min. 2D GISAXS patterns for all samples are shown in Figure S13.

that occur in the lateral structure during annealing. Using this approach, we determine typical correlation lengths for crystalline domains within our films between 1.1 and 1.2 nm (see Table 2), with such values agreeing with the manufacturer's data. Here, GISAXS measurements were designed to preferentially probe the np-SnO_2 layer averaging over the irradiated sample surface, where changes induced by annealing are most likely to be evident (our complete methodology is explained in Supporting Information note 3). From the fitted values shown in Table 2 (with further parameters presented in Table S3), thermal annealing increases the typical domain size for grains in the film from ∼1.17 to ∼1.22 nm, a result that confirms that thermal annealing increases the average size of the crystalline domains. We also determine a reduction in the Porod exponent d from ∼4 (corresponding to an ideal, smooth surface) to ∼3.6, a result

Table 2. Guinier−Porod Fitting Parameters for GISAXS Profiles of np-SnO_2 Films[a]

sample	R_g (Å^{-1})	d (Porod exponent)	fitted domain size (nm)
as deposited	9.09 ± 0.05	3.984 ± 0.31	1.173 ± 0.006
annealed	9.43 ± 0.05	3.612 ± 0.24	1.218 ± 0.006
HAF 1 min	9.27 ± 0.05	3.829 ± 0.28	1.197 ± 0.006
HAF 2 min	9.31 ± 0.05	3.831 ± 0.27	1.202 ± 0.006
HAF 5 min	9.42 ± 0.05	3.661 ± 0.24	1.216 ± 0.006

[a]Typical grain size is determined assuming spherical domains, with full details given in Supporting Information note 3.

that indicates the presence of less well-defined spherical boundaries between SnO_2 domains following annealing. Therefore, we conclude that the annealed film can be considered as a densely packed layer of spheres that become fused, with the crystalline domaincontinuing to grow during thermal annealing.

Various rapid thermal processing techniques have been used to process perovskite layers, notably photonic curing, flash infra-red annealing, intense pulsed light (IPL), and rapid thermal processing.[33−36] Such techniques have also been used to replace TiO_2 sintering;[37−39] however, the high transmissivity of thin np-SnO_2 complicates their use for this material; for example, photonic curing or extended thermal annealing will instead cause damage to flexible plastic substrates like PET or PEN. To replace thermal annealing, we have explored the use of a rapid thermal HAF process at a temperature of 120 ± 10 °C for between 1 and 5 min, as has been used to process perovskite films.[40] Here, a temperature-controlled heat gun was used to replicate the typical hot-plate thermal annealing process, representing a technique consistent with R2R processing in air. Our experimental setup is shown in Figure S14. Guinier−Porod fit parameters extracted from in-plane scatter measurements (Figure 4) from films processed using HAF show similar trends to those extracted following extended thermal annealing, with an increase in the grain radius and reduction of smoothness determined for increasing HAF process times (see Table 2). Indeed, both the Porod exponent and grain radius are found to closely match the extended annealing after only 5 min of HAF.

Post-Deposition Treatments. Various options exist to clean/process layers for R2R fabrication, including exposure to plasma. We note that the UVO system used here did not include an O_2 gas feed, so we expect that process times could be significantly reduced by including an oxygen feed or by using more intense UV light sources. UVO has been widely used as a surface treatment for SnO_2 and has been reported to enhance carrier extraction.[41] The UVO process is believed to enhance surface hydroxylation[42] (increasing the surface energy) and to reduce the surface-density of oxygen vacancies. Again, our objective is to explore an industrially applicable process, so we also investigated a 5 min O_2 plasma treatment because of its extensive use in the coating industry and explore its impact on the np-SnO_2 surface, and the SnO_2/perovskite interface. The O_2 plasma treatment combines UV cleaning under vacuum with cleaning by various ionized oxygen species. In optoelectronic devices, this has been used to modify surface electronic properties for enhanced carrier injection or extraction.[43,44]

We first investigated the effect of removing the thermal annealing process on device performance. Here, PV devices

https://dx.doi.org/10.1021/acsaem.0c00525
ACS Appl. Energy Mater. XXXX, XXX, XXX−XXX

were prepared by either drying np-SnO_2 in air or by using a one-minute annealing step at 120 °C to match the fastest HAF process that would be compatible with processing on a flexible substrate. In each case, a further 15 min UVO (here termed "120 + UVO") or O_2 plasma (termed "120 + O_2") post-treatment was applied to the np-SnO_2 ETL to understand its effect on cell performance. Table S4 shows device efficiencies following each treatment, with optimum device performance achieved using the 120 + UVO process, where a maximum reverse sweep PCE of 18.9% was recorded (champion device shown in Figure 5). This encouraging result suggests that high

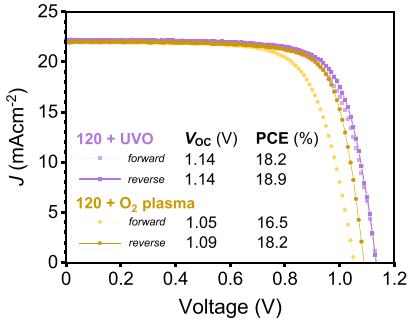

Figure 5. $J-V$ curves for the best-performing cells using np-SnO_2 treated with 1 min 120 °C drying and either 15 min UVO or 5 min O_2 plasma prior to perovskite deposition. Key sweep parameters are inset (full parameters in Table S4), with the O_2 plasma-treated np-SnO_2 device exhibiting lower V_{OC} and increased hysteresis.

performance can be achieved using both reduced processing time and relatively low annealing temperatures, with even brief annealing having performance benefit. Table S4 also indicates a reduction in V_{OC} by around 80 mV for devices treated using O_2 plasma compared with those treated using UVO (average ~1.05 V compared with ~1.13 V, respectively). This reduction is accompanied by an increase in hysteresis during scanning, where the $J-V$ sweep for the best-performing 120 + O_2 device (see Figure 5) shows a significant difference in the forward and reverse sweep PCE, V_{OC}, and FF compared with that processed using the 120 + UVO np-SnO_2.

To first confirm whether these changes in device performance result from changes in the perovskite deposited on the treated surfaces, we performed white light absorption and steady-state photoluminescence (SSPL) measurements on bilayer np-SnO_2/perovskite samples, with np-SnO_2 exposed to various processing conditions. Figure S15 shows the optical density for np-SnO_2/perovskite samples and corresponding Tauc-like plots where we assume a direct band gap. In all cases, films were found to have a similar optical band gap of ~1.62 eV, corresponding well with PL emission (see Figure S16) at ~1.63 eV in all the samples (Table S5). To further confirm whether changes observed in device performance are due to changes in the perovskite layer, we recorded grazing-incidence wide-angle X-ray scattering (GIWAXS) patterns for samples using np-SnO_2 substrates with either the 120 + UVO or 120 + O_2 plasma treatment (Figure S17). Here, we found no substrate-dependent effects on the perovskite crystallinity or orientation. From these observations, we conclude that the perovskite bulk composition and structure is comparable in both cases, irrespective of the np-SnO_2 layer treatment, a result that suggests that the observed changes in device performance result from modification at the SnO_2/perovskite interface.

Photoelectron Spectroscopy. To investigate the effect of UVO and O_2 plasma treatments on the band structure and composition of the np-SnO_2, we performed ultraviolet (UPS) and X-ray (XPS) photoelectron spectroscopy measurements. These highly surface sensitive techniques give a wealth of information on the electronic nature of surfaces and interfaces, with many reports investigating doped and undoped SnO_x for many applications, from TCOs to gas sensing.[45−48] Here, we prepared np-SnO_2 films on ITO at the same thickness as used in completed devices. XPS and UPS measurements will also include the effect of surface contaminants and adsorbates, which will be heavily dependent on the SnO_2 surface.[49] Samples might typically be prepared by thorough cleaning, followed by Ar^+ sputtering to remove adventitious carbon or other detectable species, and remain under high vacuum after preparation.[50] Here, however, cleaning/sputtering of the SnO_2 will affect its surface composition,[51] so following UVO or O_2 treatments in air, samples were sealed under vacuum and then rapidly transferred to high vacuum for the measurements.

By measuring XPS spectra across an extended binding energy range, we investigate the surface elemental composition of the np-SnO_2 layers. We note that the np-SnO_2 suspension used here is stabilized using KOH (with a solution pH of ~11.5, see Figure S18). From survey (wide) scan spectra shown in Figure S19, we find that the O_2 plasma-treated samples are characterized by reduced emission from K 2p core levels and weakly detectable emission from In 3d levels. This indicates that the O_2 plasma partially removes KOH from the np-SnO_2 surface, and also etches the np-SnO_2 layer, allowing indium in the ITO substrate to be detected. We also find significantly increased F 1s intensity which we attribute to fluorine contamination arising from degraded PTFE coatings within the plasma reactor.[52] Indeed, if fluorine is incorporated into the SnO_2 surface, it may increase the optical band gap.[53] We also compared the effect of each processing step on the adventitious carbon with C 1s core-level spectra (see Figure S20). As expected, we found that annealing does not remove carbon contaminants, whereas UVO and O_2 plasma both significantly reduce carbon species present at the surface.

Various other stable adsorbates are expected to be present at SnO_2 surfaces, notably O_2, H_2O, and hydroxide species, with their concentration heavily dependent on the SnO_2 surface and stoichiometry.[49,54,55] We probed the O 1s core-level XPS emission to understand changes in surface oxygen species, with spectra and fits for 120 + UVO and 120 + O_2 plasma shown in Figure S21. Two components were fitted (in most cases) using a lower energy feature having a binding energy of 531.1−531.3 eV together with a higher energy shoulder at 532.4−532.6 eV (fitting methodology is described in the experimental methods). The peak at 531.2 eV is ascribed to lattice oxygen (O−Sn bonds) with the second broader feature originating from adsorbed species such as −OH groups and carbonates.[55,56] In the O_2 plasma-treated samples, a distinct third peak was detected at 533.3 eV which we suspect is related to an additional adsorbate species induced by fluorine modifying the surface.[57] In Table S6, we compare the relative areas of O 1s and Sn 3d and find that annealed and 120 + UVO samples have the highest area ratio for both [O 1s]/[Sn 3d] and Sn−O/[Sn 3d], which is reduced following an O_2 plasma treatment. While these values should be treated with caution because of the effect of adsorbates, our results suggest that 5 min of O_2 plasma treatment can significantly modify the surface species, apparently leading to an Sn-rich, O-poor

https://dx.doi.org/10.1021/acsaem.0c00525
ACS Appl. Energy Mater. XXXX, XXX, XXX−XXX

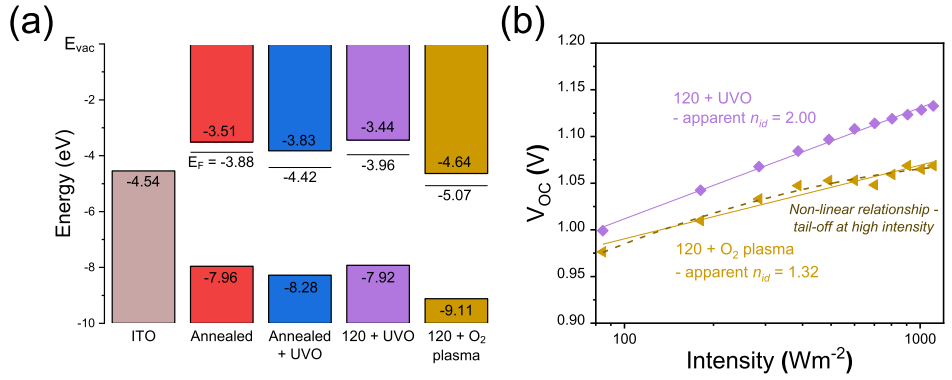

Figure 6. Understanding the effect of UVO and O_2 plasma treatments. (a) Electronic structure at the np-SnO_2 surface with the Fermi level (E_F) from UPS measurements, valence band from UPS and XPS and estimated conduction band from the optical band gap. (b) Stabilized light-V_{OC} measurements for 120 + UVO and 120 + O_2 devices, showing reduced V_{OC} for the plasma treatment. Apparent n_{id} from linear fits are shown, and in the O_2 plasma case, behavior indicates increased nonradiative recombination at the ETL interface.[64,67]

surface.[58] A reduced O/Sn ratio has previously been observed following an O_2 plasma treatment,[59] but the reverse has also been reported for reduced SnO_2 surfaces.[60] In summary, the SnO_2 surface following the treatment will be impacted by the initial stoichiometry and crystallinity of the surface, the proportion of different ionized oxygen species in the plasma, the nature of fluorine contamination, and the process duration.[49,53]

To analyze the electronic structure from UPS spectra, the secondary electron edge (or E_{cutoff}) was used to determine the work function (WF) for each layer, with the onset energy (E_{onset}) used to find the valence band maximum (VBM) with respect to the Fermi level (E_F) (see Figure S22). To confirm the VBM positions (ionisation energy, I_E) for all samples, we also extracted E_{onset} values from XPS valence spectra (see Figure S23). These values agreed with those determined from UPS measurements (see Tables S5 and S6). As noted above, the energy-level determination will be affected by extrinsic band bending because of adsorbates, with adsorbed moisture expected to lead to the formation of an accumulation layer at the SnO_2/perovskite interface.[54] Noting this, we show an apparent energy level diagram for ITO and key np-SnO_2 samples in Figure 6a, illustrating the position of the Fermi level, the VBM and estimated conduction band minimum (CBM) using our previously determined optical band gap values for np-SnO_2 (Figure S24 illustrates the energy level determination). Here, it is immediately apparent that the O_2 plasma treatment has caused a significant shift of the Fermi level and ionization energy. Changes to the chemical species present, together with a reduced layer thickness and modified oxidation state have significantly altered the surface of the 120 + O_2 sample surface, a conclusion confirmed by the "as-deposited + O_2" sample exhibiting similarly shifted energy levels (see Table S7). We note that this is consistent with literature reports on TCOs treated with O_2 plasma, a process that has been shown to downshift the Fermi level in FTO and ITO surfaces by 0.5−0.6 eV.[43,49] We also note that the energy levels determined for the annealed sample are significantly modified following the UVO treatment, an observation that may partly result from removal of carbon species, as identified in Figure S20. For completeness, we give typical triple cation perovskite and spiro-OMeTAD energy levels (predominantly measured by UPS at the top surface combined with optical bandgap) in Table S9, with the triple-cation perovskite CBM typically in the range −3.79 to −4.46 eV.

Device Physics. Previous work has shown that the illumination intensity-dependent variation of V_{OC} can provide information about the dominant recombination mechanisms in photovoltaic devices. Classically, the light ideality factor (n_{id}) extracted using this approach determines whether recombination is primarily bimolecular (band-to-band) or monomolecular (trap-assisted), in cases with comparable electron and hole densities.[61,62] With varied carrier densities, trap energies and trap locations (bulk or interface), n_{id} can take a range of values ($n_{id} \approx 1-2$); analysis is complicated in hybrid perovskite devices by the influence of mobile ions, which lead to transient modification of interfaces, and therefore carrier extraction behavior.[62,63] Adopting the approach modeled by Tress *et al.*, we recorded stabilized V_{OC} measurements after a set illumination period and found that the 120 + O_2 sample exhibits behavior consistent with poor charge selectivity (see Figure 6b).[64] This result suggests increased interface recombination in this case despite a lower apparent n_{id} extracted from a linear fit (1.32 compared to 2.00 in the 120 + UVO sample). Transient photovoltage measurements recorded at 1 sun are shown in Figure S25 and show slower voltage stabilization for O_2 plasma-treated devices. Over tens of seconds, these changes in V_{OC} are likely to result from dynamic processes at the ETL interface caused by the interaction of both mobile ions and charge carriers, modifying carrier extraction behaviour.[63,65]

Therefore, we conclude that the observed V_{OC} loss shown in Figure 5 and Table S4 for devices utilizing the 120 + O_2 ETL results from a significant modification of the surface chemistry. This leads to an apparent downshift of the VBM, Fermi level, and CBM of the SnO_2, resulting in a loss of electron selectivity, with reduced quasi-Fermi level splitting in the device. While the observed energy shifts are significant, they are affected by adsorbates which also affect the extrinsic electron density at the interface and may even evolve dynamically under operation.[54,55] However, it is clear that both misalignment and modified doping density will change the charge and ionic screening behavior of the interface, a process that most likely causes the increased hysteresis observed in O_2 plasma-treated samples.[66] However, it is unclear whether band alignment and doping effects can be independently modified with O_2 plasma.[30,67] It has also been reported that ALD SnO_2 with different oxidants (such as O_2 plasma or ozone) can lead to changes in the electronic properties of the ETL layer, as well as modifying the subsequent perovskite growth,[68] a process that

https://dx.doi.org/10.1021/acsaem.0c00525
ACS Appl. Energy Mater. XXXX, XXX, XXX−XXX

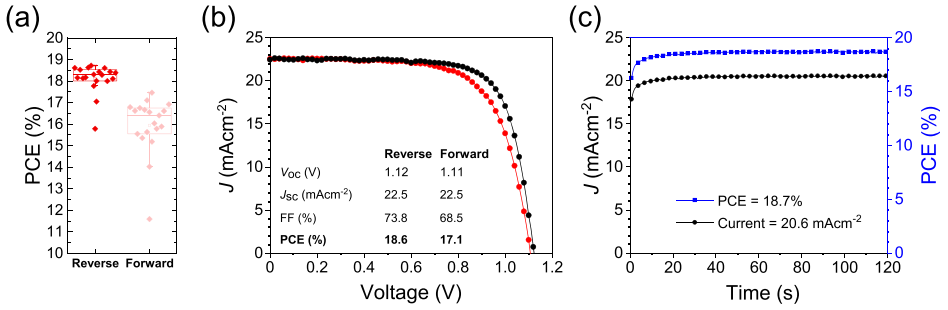

Figure 7. Photovoltaic performance for devices prepared using fast processing: spray coating, 1 min HAF, and UVO treatment. (a) Reverse and forward sweep efficiencies for 19 operational cells, (b) $J-V$ sweep, and (c) SPO of the best-performing cell.

Table 3. Fast-Processed Device Performance Using Sprayed np-SnO_2, 1 min HAF and UVO Treatment

coating	treatment	sweep	PCE (%)	J_{SC} (mA cm^{-2})	V_{OC}	FF	no. of cells
spray	HAF 1 min + UVO	forward	17.11 (15.95 ± 1.29)	22.55 (22.54 ± 0.18)	1.11 (1.09 ± 0.03)	68.52 (65.08 ± 3.62)	19
		reverse	18.62 (18.11 ± 0.66)	22.45 (22.55 ± 0.17)	1.12 (1.11 ± 0.01)	73.81 (72.32 ± 1.93)	

may also be influenced by the observed reduction in KOH.[26] It is clear that further research is needed to characterize chemical reactivity between different substrate transport materials and the perovskite layer during film formation.[9,68]

Overall, it is evident that O_2 plasma can have a detrimental impact on the SnO_2/perovskite interface if not properly controlled; however, promising results using shorter treatment times have been achieved.[69] Surface preparation equipment (both UVO and O_2 plasma) used in research contexts varies greatly in device performance, power and process control, making exact methods difficult to reproduce between laboratories. As such, further efforts must be made to replicate industrially relevant plasma cleaning approaches used in interface preparation.

Rapid Processing. Combining the optimized spray coating, 1 min HAF, and UVO treatment, PV devices were prepared using this series of processes that have the potential to be fully transferrable to R2R or other low-cost processing. In Figure 7, we show a histogram of all device efficiencies, as well as the current−voltage performance and SPO for the champion device with a stabilized PCE of 18.7%. To accompany this, average and champion performance parameters are shown in Table 3, showing comparable metrics to annealed spin- and spray-coated devices presented earlier, although with increased hysteresis and slightly reduced average V_{OC} and FF. The total processing time here is around 1 min (mainly determined by the annealing step), with spatial atomic layer deposition (SALD) being the only comparably rapid, low-temperature deposition technique that operates in an ambient atmosphere able to create functional SnO_x layers for applications in perovskite solar cells. We note that Hoffmann *et al.* fabricated p−i−n devices incorporating a SnO_x ETL (that also acted as an impermeable barrier layer), with devices with over 12% PCE. Here, devices were fabricated using a substrate processing speed and temperature of 20−80 mm s^{-1} and 80 °C, respectively (compared with 25 °C and up to 180 mm s^{-1} achieved in our process), but with no further annealing required.[70]

CONCLUSIONS

We have explored the deposition of SnO_2 nanoparticle layers using two scalable deposition processes (spray coating and slot-die coating) and fabricated perovskite devices with performance and morphology comparable to those of spin-coating. The effect of annealing is investigated using GISAXS, where we quantify the fusing of nanoparticles into a densely packed ETL. The effect of annealing, UV ozone, and O_2 plasma post-treatments were also investigated using UPS, XPS, optical, and electrical measurements. We observed significant modification to adsorbed species, concomitant with shifts of apparent np-SnO_2 energy levels. Using an O_2 plasma treatment, a significant reduction in the Fermi level led to a loss of V_{OC} and increased current−voltage hysteresis. Finally, we demonstrated an optimized fast deposition technique involving annealing the SnO_2 layer in hot air to create photovoltaic devices yielding stabilized power conversion efficiencies close to 19%. This work outlines the future design requirements for rapid processing of functional metal oxide nanoparticle layers, deposited at high speed and under ambient conditions—conditions compatible with R2R processing.

ASSOCIATED CONTENT

Supporting Information

The Supporting Information is available free of charge at https://pubs.acs.org/doi/10.1021/acsaem.0c00525.

Experimental methods, notes on solvent mixtures, band-fluctuation modeling and GISAXS modeling; extended device performance data, process images and diagrams, ellipsometry, contact angle measurements, additional AFM, PL, absorption, Tauc plots, GIWAXS, XPS spectra, UPS spectra, energy-level determination, and photovoltage measurements; further device metrics, Guinier−Porod fitting, XPS fits, electronic structure determination, and energy levels (PDF)

AUTHOR INFORMATION

Corresponding Author

David G. Lidzey − *Department of Physics & Astronomy, University of Sheffield, Sheffield S3 7RH, U.K.;* orcid.org/0000-0002-8558-1160; Email: d.g.lidzey@sheffield.ac.uk

Authors

Joel A. Smith − *Department of Physics & Astronomy, University of Sheffield, Sheffield S3 7RH, U.K.;* orcid.org/0000-0001-6889-4408

https://dx.doi.org/10.1021/acsaem.0c00525
ACS Appl. Energy Mater. XXXX, XXX, XXX−XXX

Onkar S. Game − *Department of Physics & Astronomy, University of Sheffield, Sheffield S3 7RH, U.K.;* orcid.org/0000-0002-5573-3602
James E. Bishop − *Department of Physics & Astronomy, University of Sheffield, Sheffield S3 7RH, U.K.*
Emma L. K. Spooner − *Department of Physics & Astronomy, University of Sheffield, Sheffield S3 7RH, U.K.;* orcid.org/0000-0001-9575-550X
Rachel C. Kilbride − *Department of Physics & Astronomy, University of Sheffield, Sheffield S3 7RH, U.K.;* orcid.org/0000-0002-3985-923X
Claire Greenland − *Department of Physics & Astronomy, University of Sheffield, Sheffield S3 7RH, U.K.;* orcid.org/0000-0002-9644-8672
Rahul Jayaprakash − *Department of Physics & Astronomy, University of Sheffield, Sheffield S3 7RH, U.K.;* orcid.org/0000-0002-2021-1601
Tarek I. Alanazi − *Department of Physics & Astronomy, University of Sheffield, Sheffield S3 7RH, U.K.; Department of Physics, College of Science, Northern Border University, Arar 73222, Kingdom of Saudi Arabia;* orcid.org/0000-0001-8843-0969
Elena J. Cassella − *Department of Physics & Astronomy, University of Sheffield, Sheffield S3 7RH, U.K.;* orcid.org/0000-0003-4897-1650
Alvaro Tejada − *Institut für Silizium-Photovoltaik, Helmholtz-Zentrum Berlin für Materialien und Energie GmbH, Berlin 12489, Germany; Departamento de Ciencias, Sección Física, Pontificia Universidad Católica del Perú, Lima 32, Peru*
Ganna Chistiakova − *Institut für Silizium-Photovoltaik, Helmholtz-Zentrum Berlin für Materialien und Energie GmbH, Berlin 12489, Germany*
Michael Wong-Stringer − *Department of Physics & Astronomy, University of Sheffield, Sheffield S3 7RH, U.K.;* orcid.org/0000-0002-4364-4127
Thomas J. Routledge − *Department of Physics & Astronomy, University of Sheffield, Sheffield S3 7RH, U.K.;* orcid.org/0000-0003-0890-113X
Andrew J. Parnell − *Department of Physics & Astronomy, University of Sheffield, Sheffield S3 7RH, U.K.;* orcid.org/0000-0001-8606-8644
Deborah B. Hammond − *Department of Chemistry, University of Sheffield, Sheffield S3 7HF, U.K.;* orcid.org/0000-0003-3785-2947

Complete contact information is available at: https://pubs.acs.org/10.1021/acsaem.0c00525

Notes

The authors declare the following competing financial interest(s): D.G.L. is a co-director of the company Ossila that retail materials and equipment used in perovskite photovoltaic device research and development.

■ ACKNOWLEDGMENTS

We thank the EPSRC for PhD studentships through the Centre for Doctoral Training in New and Sustainable PV, EP/L01551X/1 (J.A.S., E.L.K.S., C.G.) and *via* the University of Sheffield DTG account (J.E.B., R.C.K.). T.I.A. thanks the Saudi Government for funding *via* a PhD studentship. We also acknowledge funding from EPSRC to support this work *via* grants "Hybrid Polaritonics" (EP/M025330/1), "High-resolution mapping of performance and degradation mechanisms in printable photovoltaic devices" (EP/M025020/1), "The integration of photovoltaic devices with carbon-fibre composites" (EP/S009213/1) and from the Global Challenges Research Fund (GCRF) through Science and Technology Facilities Council (STFC), grant number ST/R002754/1 "Synchrotron Techniques for African Research and Technology (START)". J.A.S. also thanks the Erasmus + exchange program for support. We also thank Thomas Featherstone for assistance with XPS data analysis, Carolin Rehermann for helping with UV−Vis measurements, as well as Selina Olthof and Aboma Merdasa for useful discussions. The XPS instrument belongs to the Sheffield Surface Analysis Centre, a facility run from the Department of Chemistry, University of Sheffield, and is led by Professor Graham Leggett. We thank the company Xenocs for their help and ongoing support in the X-ray scattering user program at Sheffield, and we thank the EPSRC for funding the purchase of this instrument.

■ REFERENCES

(1) Kojima, A.; Teshima, K.; Shirai, Y.; Miyasaka, T. Organometal Halide Perovskites as Visible-Light Sensitizers for Photovoltaic Cells. *J. Am. Chem. Soc.* **2009**, *131*, 6050−6051.
(2) NREL. Best Research-Cell Efficiencies. https://www.nrel.gov/pv/cell-efficiency.html (accessed Dec 10, 2019).
(3) Stranks, S. D. Nonradiative Losses in Metal Halide Perovskites. *ACS Energy Lett.* **2017**, *2*, 1515−1525.
(4) Egger, D. A.; Bera, A.; Cahen, D.; Hodes, G.; Kirchartz, T.; Kronik, L.; Lovrincic, R.; Rappe, A. M.; Reichman, D. R.; Yaffe, O. What Remains Unexplained about the Properties of Halide Perovskites? *Adv. Mater.* **2018**, *30*, 1800691.
(5) Saliba, M.; Matsui, T.; Seo, J.-Y.; Domanski, K.; Correa-Baena, J.-P.; Nazeeruddin, M. K.; Zakeeruddin, S. M.; Tress, W.; Abate, A.; Hagfeldt, A.; Grätzel, M. Cesium-Containing Triple Cation Perovskite Solar Cells: Improved Stability, Reproducibility and High Efficiency. *Energy Environ. Sci.* **2016**, *9*, 1989−1997.
(6) Berhe, T. A.; Su, W.-N.; Chen, C.-H.; Pan, C.-J.; Cheng, J.-H.; Chen, H.-M.; Tsai, M.-C.; Chen, L.-Y.; Dubale, A. A.; Hwang, B.-J. Organometal Halide Perovskite Solar Cells: Degradation and Stability. *Energy Environ. Sci.* **2016**, *9*, 323−356.
(7) Leijtens, T.; Eperon, G. E.; Pathak, S.; Abate, A.; Lee, M. M.; Snaith, H. J. Overcoming Ultraviolet Light Instability of Sensitized TiO_2 with Meso-Superstructured Organometal Tri-Halide Perovskite Solar Cells. *Nat. Commun.* **2013**, *4*, 2885.
(8) Ke, W.; Fang, G.; Liu, Q.; Xiong, L.; Qin, P.; Tao, H.; Wang, J.; Lei, H.; Li, B.; Wan, J.; Yang, G.; Yan, Y. Low-Temperature Solution-Processed Tin Oxide as an Alternative Electron Transporting Layer for Efficient Perovskite Solar Cells. *J. Am. Chem. Soc.* **2015**, *137*, 6730−6733.
(9) Christians, J. A.; Schulz, P.; Tinkham, J. S.; Schloemer, T. H.; Harvey, S. P.; Tremolet de Villers, B. J.; Sellinger, A.; Berry, J. J.; Luther, J. M. Tailored Interfaces of Unencapsulated Perovskite Solar Cells for >1,000 Hour Operational Stability. *Nat. Energy* **2018**, *3*, 68−74.
(10) Tiwana, P.; Docampo, P.; Johnston, M. B.; Snaith, H. J.; Herz, L. M. Electron Mobility and Injection Dynamics in Mesoporous ZnO, SnO_2, and TiO_2 Films Used in Dye-Sensitized Solar Cells. *ACS Nano* **2011**, *5*, 5158−5166.
(11) Baena, J. P. C.; Steier, L.; Tress, W.; Saliba, M.; Neutzner, S.; Matsui, T.; Giordano, F.; Jacobsson, T. J.; Kandada, A. R. S.; Zakeeruddin, S. M.; Petrozza, A.; Abate, A.; Nazeeruddin, M. K.; Grätzel, M.; Hagfeldt, A. Highly Efficient Planar Perovskite Solar Cells through Band Alignment Engineering. *Energy Environ. Sci.* **2015**, *8*, 2928−2934.
(12) Dong, Q.; Shi, Y.; Wang, K.; Li, Y.; Wang, S.; Zhang, H.; Xing, Y.; Du, Y.; Bai, X.; Ma, T. Insight into Perovskite Solar Cells Based on SnO_2 Compact Electron-Selective Layer. *J. Phys. Chem. C* **2015**, *119*, 10212−10217.

(13) Bush, K. A.; Palmstrom, A. F.; Yu, Z.; Boccard, M.; Cheacharoen, R.; Mailoa, J. P.; McMeekin, D. P.; Hoye, R. L. Z.; Bailie, C. D.; Leijtens, T.; Peters, I. M.; Minichetti, M. C.; Rolston, N.; Prasanna, R.; Sofia, S. E.; Harwood, D.; Ma, W.; Moghadam, F.; Snaith, H. J.; Buonassisi, T.; Holman, Z. C.; Bent, S. F.; McGehee, M. D. 23.6%-Efficient Monolithic Perovskite/Silicon Tandem Solar Cells with Improved Stability. *Nat. Energy* **2017**, *2*, 17009.
(14) Wang, C.; Zhao, D.; Grice, C. R.; Liao, W.; Yu, Y.; Cimaroli, A.; Shrestha, N.; Roland, P. J.; Chen, J.; Yu, Z.; Liu, P.; Cheng, N.; Ellingson, R. J.; Zhao, X.; Yan, Y. Low-Temperature Plasma-Enhanced Atomic Layer Deposition of Tin Oxide Electron Selective Layers for Highly Efficient Planar Perovskite Solar Cells. *J. Mater. Chem. A* **2016**, *4*, 12080−12087.
(15) Ma, J.; Zheng, X.; Lei, H.; Ke, W.; Chen, C.; Chen, Z.; Yang, G.; Fang, G. Highly Efficient and Stable Planar Perovskite Solar Cells With Large-Scale Manufacture of E-Beam Evaporated SnO_2 Toward Commercialization. *Sol. RRL* **2017**, *1*, 1700118.
(16) Guo, Y.; Yin, X.; Liu, J.; Chen, W.; Wen, S.; Que, M.; Xie, H.; Yang, Y.; Que, W.; Gao, B. Vacuum Thermal-Evaporated SnO_2 as Uniform Electron Transport Layer and Novel Management of Perovskite Intermediates for Efficient and Stable Planar Perovskite Solar Cells. *Org. Electron.* **2019**, *65*, 207−214.
(17) Qiu, L.; Liu, Z.; Ono, L. K.; Jiang, Y.; Son, D. Y.; Hawash, Z.; He, S.; Qi, Y. Scalable Fabrication of Stable High Efficiency Perovskite Solar Cells and Modules Utilizing Room Temperature Sputtered SnO2 Electron Transport Layer. *Adv. Funct. Mater.* **2019**, *29*, 1806779.
(18) Anaraki, E. H.; Kermanpur, A.; Steier, L.; Domanski, K.; Matsui, T.; Tress, W.; Saliba, M.; Abate, A.; Grätzel, M.; Hagfeldt, A.; Correa-Baena, J.-P. Highly Efficient and Stable Planar Perovskite Solar Cells by Solution-Processed Tin Oxide. *Energy Environ. Sci.* **2016**, *9*, 3128−3134.
(19) Jiang, Q.; Zhang, L.; Wang, H.; Yang, X.; Meng, J.; Liu, H.; Yin, Z.; Wu, J.; Zhang, X.; You, J. Enhanced Electron Extraction Using SnO_2 for High-Efficiency Planar-Structure $HC(NH_2)_2PbI_3$-Based Perovskite Solar Cells. *Nat. Energy* **2017**, *2*, 16177.
(20) Duan, J.; Xiong, Q.; Feng, B.; Xu, Y.; Zhang, J.; Wang, H. Low-Temperature Processed SnO_2 Compact Layer for Efficient Mesostructure Perovskite Solar Cells. *Appl. Surf. Sci.* **2017**, *391*, 677−683.
(21) Roose, B.; Baena, J.-P. C.; Gödel, K. C.; Graetzel, M.; Hagfeldt, A.; Steiner, U.; Abate, A. Mesoporous SnO_2 Electron Selective Contact Enables UV-Stable Perovskite Solar Cells. *Nano Energy* **2016**, *30*, 517−522.
(22) Li, Y.; Zhu, J.; Huang, Y.; Liu, F.; Lv, M.; Chen, S.; Hu, L.; Tang, J.; Yao, J.; Dai, S. Mesoporous SnO_2 Nanoparticle Films as Electron-Transporting Material in Perovskite Solar Cells. *RSC Adv.* **2015**, *5*, 28424−28429.
(23) Jiang, Q.; Zhao, Y.; Zhang, X.; Yang, X.; Chen, Y.; Chu, Z.; Ye, Q.; Li, X.; Yin, Z.; You, J. Surface Passivation of Perovskite Film for Efficient Solar Cells. *Nat. Photonics* **2019**, *13*, 460−466.
(24) Ding, J.; Han, Q.; Ge, Q.-Q.; Xue, D.; Ma, J.-Y.; Zhao, B.; Chen, Y.-X.; Liu, J.; Mitzi, D. B.; Hu, J.-S. Fully Air-Bladed High-Efficiency Perovskite Photovoltaics. *Joule* **2019**, *3*, 402.
(25) Dou, B.; Whitaker, J. B.; Bruening, K.; Moore, D. T.; Wheeler, L. M.; Ryter, J.; Breslin, N. J.; Berry, J. J.; Garner, S. M.; Barnes, F. S.; Shaheen, S. E.; Tassone, C. J.; Zhu, K.; van Hest, M. F. A. M.; Sean, E.; Tassone, C. J.; Zhu, K.; Hest, M. F. A. M. Van. Roll-to-Roll Printing of Perovskite Solar Cells. *ACS Energy Lett.* **2018**, *3*, 2558−2565.
(26) Bu, T.; Li, J.; Zheng, F.; Chen, W.; Wen, X.; Ku, Z.; Peng, Y.; Zhong, J.; Cheng, Y.-B.; Huang, F. Universal Passivation Strategy to Slot-Die Printed SnO_2 for Hysteresis-Free Efficient Flexible Perovskite Solar Module. *Nat. Commun.* **2018**, *9*, 4609.
(27) Bishop, J. E.; Routledge, T. J.; Lidzey, D. G. Advances in Spray-Cast Perovskite Solar Cells. *J. Phys. Chem. Lett.* **2018**, *9*, 1977−1984.
(28) Bishop, J. E.; Smith, J. A.; Greenland, C.; Kumar, V.; Vaenas, N.; Game, O. S.; Routledge, T. J.; Wong-Stringer, M.; Rodenburg, C.; Lidzey, D. G. High-Efficiency Spray-Coated Perovskite Solar Cells Utilizing Vacuum-Assisted Solution Processing. *ACS Appl. Mater. Interfaces* **2018**, *10*, 39428−39434.
(29) Mathies, F.; Eggers, H.; Richards, B. S.; Hernandez-Sosa, G.; Lemmer, U.; Paetzold, U. W. Inkjet-Printed Triple Cation Perovskite Solar Cells. *ACS Appl. Energy Mater.* **2018**, *1*, 1834−1839.
(30) Yun, A. J.; Kim, J.; Hwang, T.; Park, B. Origins of Efficient Perovskite Solar Cells with Low-Temperature Processed SnO_2 Electron Transport Layer. *ACS Appl. Energy Mater.* **2019**, *2*, 3554−3560.
(31) Guerra, J. A.; Tejada, A.; Töfflinger, J. A.; Grieseler, R.; Korte, L. Band-Fluctuations Model for the Fundamental Absorption of Crystalline and Amorphous Semiconductors: A Dimensionless Joint Density of States Analysis. *J. Phys. D: Appl. Phys.* **2019**, *52*, 105303.
(32) Hammouda, B. A New Guinier-Porod Model. *J. Appl. Crystallogr.* **2010**, *43*, 716−719.
(33) Troughton, J.; Carnie, M. J.; Davies, M. L.; Charbonneau, C.; Jewell, E. H.; Worsley, D. A.; Watson, T. M. Photonic Flash-Annealing of Lead Halide Perovskite Solar Cells in 1 ms. *J. Mater. Chem. A* **2016**, *4*, 3471−3476.
(34) Sanchez, S.; Hua, X.; Phung, N.; Steiner, U.; Abate, A. Flash Infrared Annealing for Antisolvent-Free Highly Efficient Perovskite Solar Cells. *Adv. Energy Mater.* **2018**, *8*, 1702915.
(35) Ghahremani, A. H.; Martin, B.; Gupta, A.; Bahadur, J.; Ankireddy, K.; Druffel, T. Rapid Fabrication of Perovskite Solar Cells through Intense Pulse Light Annealing of SnO_2 and Triple Cation Perovskite Thin Films. *Mater. Des.* **2020**, *185*, 108237.
(36) Ouyang, Z.; Yang, M.; Whitaker, J. B.; Li, D.; van Hest, M. F. A. M. Towards Scalable Perovskite Solar Modules Using Blade-Coating and Rapid Thermal Processing. *ACS Appl. Energy Mater.* **2020**, *3*, 3714.
(37) Charbonneau, C.; Holliman, P. J.; Davies, M. L.; Watson, T. M.; Worsley, D. A. Facile Self-Assembly and Stabilization of Metal Oxide Nanoparticles. *J. Colloid Interface Sci.* **2015**, *442*, 110−119.
(38) Das, S.; Gu, G.; Joshi, P. C.; Yang, B.; Aytug, T.; Rouleau, C. M.; Geohegan, D. B.; Xiao, K. Low Thermal Budget, Photonic-Cured Compact TiO_2 Layers for High-Efficiency Perovskite Solar Cells. *J. Mater. Chem. A* **2016**, *4*, 9685−9690.
(39) Feleki, B.; Bex, G.; Andriessen, R.; Galagan, Y.; Di Giacomo, F. Rapid and Low Temperature Processing of Mesoporous TiO_2 for Perovskite Solar Cells on Flexible and Rigid Substrates. *Mater. Today Commun.* **2017**, *13*, 232−240.
(40) Liu, Y.; Shin, I.; Hwang, I.-W.; Lee, J.; Kim, S.; Lee, D. Y.; Lee, S.-H.; Jang, J.-W.; Jung, Y. K.; Jeong, J. H.; Park, S. H.; Kim, K. H. Effective Hot-Air Annealing for Improving the Performance of Perovskite Solar Cells. *Sol. Energy* **2017**, *146*, 359−367.
(41) Dong, Q.; Shi, Y.; Zhang, C.; Wu, Y.; Wang, L. Energetically Favored Formation of SnO_2 Nanocrystals as Electron Transfer Layer in Perovskite Solar Cells with High Efficiency Exceeding 19%. *Nano Energy* **2017**, *40*, 336−344.
(42) Méndez, P. F.; Muhammed, S. K. M.; Barea, E. M.; Masi, S.; Mora-Seró, I. Analysis of the UV−Ozone-Treated SnO_2 Electron Transporting Layer in Planar Perovskite Solar Cells for High Performance and Reduced Hysteresis. *Sol. RRL* **2019**, *3*, 1900191.
(43) Milliron, D. J.; Hill, I. G.; Shen, C.; Kahn, A.; Schwartz, J. Surface Oxidation Activates Indium Tin Oxide for Hole Injection. *J. Appl. Phys.* **2000**, *87*, 572−576.
(44) Lee, K. H.; Jang, H. W.; Kim, K.-B.; Tak, Y.-H.; Lee, J.-L. Mechanism for the Increase of Indium-Tin-Oxide Work Function by O_2 Inductively Coupled Plasma Treatment. *J. Appl. Phys.* **2004**, *95*, 586.
(45) Themlin, J. M.; Sporken, R.; Darville, J.; Caudano, R.; Gilles, J. M.; Johnson, R. L. Resonant-Photoemission Study of SnO_2: Cationic Origin of the Defect Band-Gap States. *Phys. Rev. B: Condens. Matter Mater. Phys.* **1990**, *42*, 11914−11925.
(46) McGuinness, C.; Stagarescu, C. B.; Ryan, P. J.; Downes, J. E.; Fu, D.; Smith, K. E.; Egdell, G. Influence of Shallow Core-Level Hybridization on the Electronic Structure of Post-Transition-Metal Oxides Studied Using Soft X-Ray Emission and Absorption. *Phys. Rev. B: Condens. Matter Mater. Phys.* **2003**, *68*, 165104.

https://dx.doi.org/10.1021/acsaem.0c00525
ACS Appl. Energy Mater. XXXX, XXX, XXX−XXX

(47) Batzill, M. Surface Science Studies of Gas Sensing Materials: SnO_2. *Sensors* **2006**, *6*, 1345−1366.
(48) Das, S.; Jayaraman, V. SnO2: A Comprehensive Review on Structures and Gas Sensors. *Prog. Mater. Sci.* **2014**, *66*, 112−255.
(49) Weidner, M. Fermi Level Determination in Tin Oxide by Photoelectron Spectroscopy. Ph.D. Thesis, TU Darmstadt, 2015.Thesiss
(50) Helander, M. G.; Greiner, M. T.; Wang, Z. B.; Lu, Z. H. Pitfalls in Measuring Work Function Using Photoelectron Spectroscopy. *Appl. Surf. Sci.* **2010**, *256*, 2602−2605.
(51) Egdell, R. G.; Eriksen, S.; Flavell, W. R. A Spectroscopic Study of Electron and Ion Beam Reduction of SnO_2(110). *Surf. Sci.* **1987**, *192*, 265−274.
(52) Karulkar, P. C. XPS/AES Investigation of Cross Contamination in a Plasma Etcher. *J. Vac. Sci. Technol., B: Microelectron. Nanometer Struct.* **1985**, *3*, 889.
(53) Swallow, J. E. N.; Williamson, B. A. D.; Whittles, T. J.; Birkett, M.; Featherstone, T. J.; Peng, N.; Abbott, A.; Farnworth, M.; Cheetham, K. J.; Warren, P.; Scanlon, D. O.; Dhanak, V. R.; Veal, T. D. Self-Compensation in Transparent Conducting F-Doped SnO_2. *Adv. Funct. Mater.* **2018**, *28*, 1701900.
(54) Trost, S.; Becker, T.; Polywka, A.; Görrn, P.; Oszajca, M. F.; Luechinger, N. A.; Rogalla, D.; Weidner, M.; Reckers, P.; Mayer, T.; Riedl, T. Avoiding Photoinduced Shunts in Organic Solar Cells by the Use of Tin Oxide (SnO_x) as Electron Extraction Material Instead of ZnO. *Adv. Energy Mater.* **2016**, *6*, 1600347.
(55) Roose, B.; Friend, R. H. Extrinsic Electron Concentration in SnO_2 Electron Extracting Contact in Lead Halide Perovskite Solar Cells. *Adv. Mater. Interfaces* **2019**, *6*, 1801788.
(56) Chistiakova, G.; Mews, M.; Wilks, R. G.; Bär, M.; Korte, L. In-System Photoelectron Spectroscopy Study of Tin Oxide Layers Produced from Tetrakis(Dimethylamino)Tin by Plasma Enhanced Atomic Layer Deposition. *J. Vac. Sci. Technol., A* **2018**, *36*, 02D401.
(57) Noonuruk, R.; Mekprasart, W.; Vittayakorn, N.; Sritharathikhun, J.; Pecharapa, W. Physical, Electrical and Optical Properties of F/Sb Codoped SnO_2 Synthesized Via Sonochemical Process. *Ferroelectrics* **2016**, *490*, 136−148.
(58) Jiang, J. C.; Lian, K.; Meletis, E. I. Influence of Oxygen Plasma Treatment on the Microstructure of SnO_x Thin Films. *Thin Solid Films* **2002**, *411*, 203−210.
(59) Mathur, S.; Ganesan, R.; Grobelsek, I.; Shen, H.; Ruegamer, T.; Barth, S. Plasma-Assisted Modulation of Morphology and Composition in Tin Oxide Nanostructures for Sensing Applications. *Adv. Eng. Mater.* **2007**, *9*, 658−663.
(60) Cavicchi, R.; Tarlov, M.; Semancik, S. Preparation of Well-ordered, Oxygen-rich SnO_2 (110) Surfaces via Oxygen Plasma Treatment. *J. Vac. Sci. Technol., A* **1990**, *8*, 2347−2352.
(61) Wolff, C. M.; Caprioglio, P.; Stolterfoht, M.; Neher, D. Nonradiative Recombination in Perovskite Solar Cells: The Role of Interfaces. *Adv. Mater.* **2019**, *31*, 1902762.
(62) Calado, P.; Burkitt, D.; Yao, J.; Troughton, J.; Watson, T. M.; Carnie, M. J.; Telford, A. M.; Regan, B. C. O.; Nelson, J.; Barnes, P. R. F. Identifying Dominant Recombination Mechanisms in Perovskite Solar Cells by Measuring the Transient Ideality Factor. *Phys. Rev. Appl.* **2019**, *11*, 044005.
(63) Moia, D.; Gelmetti, I.; Calado, P.; Fisher, W.; Stringer, M.; Game, O.; Hu, Y.; Docampo, P.; Lidzey, D.; Palomares, E.; Nelson, J.; Barnes, P. R. F. Ionic-to-Electronic Current Amplification in Hybrid Perovskite Solar Cells: Ionically Gated Transistor-Interface Circuit Model Explains Hysteresis and Impedance of Mixed Conducting Devices. *Energy Environ. Sci.* **2019**, *12*, 1296−1308.
(64) Tress, W.; Yavari, M.; Domanski, K.; Yadav, P.; Niesen, B.; Correa Baena, J. P.; Hagfeldt, A.; Graetzel, M. Interpretation and Evolution of Open-Circuit Voltage, Recombination, Ideality Factor and Subgap Defect States during Reversible Light-Soaking and Irreversible Degradation of Perovskite Solar Cells. *Energy Environ. Sci.* **2018**, *11*, 151−165.
(65) Walter, D.; Fell, A.; Wu, Y.; Duong, T.; Barugkin, C.; Wu, N.; White, T.; Weber, K. Transient Photovoltage in Perovskite Solar Cells: Interaction of Trap-Mediated Recombination and Migration of Multiple Ionic Species. *J. Phys. Chem. C* **2018**, *122*, 11270−11281.
(66) Courtier, N. E.; Cave, J. M.; Foster, J. M.; Walker, A. B.; Richardson, G. How Transport Layer Properties Affect Perovskite Solar Cell Performance: Insights from a Coupled Charge Transport/Ion Migration Model. *Energy Environ. Sci.* **2019**, *12*, 396−409.
(67) Aygüler, M. F.; Hufnagel, A. G.; Rieder, P.; Wussler, M.; Jaegermann, W.; Bein, T.; Dyakonov, V.; Petrus, M. L.; Baumann, A.; Docampo, P. Influence of Fermi Level Alignment with Tin Oxide on the Hysteresis of Perovskite Solar Cells. *ACS Appl. Mater. Interfaces* **2018**, *10*, 11414−11419.
(68) Hu, T.; Becker, T.; Pourdavoud, N.; Zhao, J.; Brinkmann, K. O.; Heiderhoff, R.; Gahlmann, T.; Huang, Z.; Olthof, S.; Meerholz, K.; Többens, D.; Cheng, B.; Chen, Y.; Riedl, T.; Heiderhoff, R.; Gahlmann, T.; Huang, Z.; Olthof, S.; Meerholz, K.; Többens, D.; Cheng, B.; Chen, Y.; Riedl, T. Indium-Free Perovskite Solar Cells Enabled by Impermeable Tin-Oxide Electron Extraction Layers. *Adv. Mater.* **2017**, *29*, 1606656.
(69) Luan, Y.; Yi, X.; Mao, P.; Wei, Y.; Zhuang, J.; Chen, N.; Lin, T.; Li, C.; Wang, J. High-Performance Planar Perovskite Solar Cells with Negligible Hysteresis Using 2,2,2-Trifluoroethanol-Incorporated SnO_2. *iScience* **2019**, *16*, 433−441.
(70) Hoffmann, L.; Brinkmann, K. O.; Malerczyk, J.; Rogalla, D.; Becker, T.; Theirich, D.; Shutsko, I.; Görrn, P.; Riedl, T. Spatial Atmospheric Pressure Atomic Layer Deposition of Tin Oxide as an Impermeable Electron Extraction Layer for Perovskite Solar Cells with Enhanced Thermal Stability. *ACS Appl. Mater. Interfaces* **2018**, *10*, 6006−6013.

https://dx.doi.org/10.1021/acsaem.0c00525
ACS Appl. Energy Mater. XXXX, XXX, XXX−XXX